Techniques for fast and sensitive measurements of two-dimensional birefringence distributions

Michael Shribak and Rudolf Oldenbourg

We propose image processing algorithms for measuring two-dimensional distributions of linear birefringence using a pair of variable retarders. Several algorithms that use between two and five recorded frames allow us to optimize measurements for speed, sensitivity, and accuracy. We show images of asters, which consist of radial arrays of microtubule polymers recorded with a polarized light microscope equipped with a universal compensator. Our experimental results confirm our theoretical expectations. The lowest noise level of 0.036 nm was obtained when we used the five-frame technique and four-frame algorithm without extinction setting. The two-frame technique allows us to increase the speed of measurement with acceptable image quality. © 2003 Optical Society of America

OCIS codes: 180.0180, 260.1440, 260.2130, 260.5430, 170.1530, 120.5410.

1. Introduction

Living cells and functional biological systems depend on the integrity of the molecular and higher-level architecture that supports their specific activities. The polarized light microscope has been a versatile tool to reveal the anisotropic fine structure in biological preparations that can be maintained under physiological conditions, free of exogenous dyes and fluorescent markers.[1,2] Indeed, the birefringence and dichroism of objects are sensitive indicators of structural order at dimensions much smaller than the wavelength of light, including the level of atomic bonds and molecular shapes.

In functional biological systems, the birefringence or dichroism can vary rapidly in time and space revealing the subtle changes in molecular arrangements occurring at a submicroscopic scale. The techniques for fast and sensitive measurements of two-dimensional birefringence patterns have significantly improved during the past two decades. In the mid-1990s, imaging measurement systems with rotated optical polarization elements were reported.[3–8] Devices with a variable retarder and beam splitting[9,10] and with return-path techniques[11,12] were also proposed. Here we report on improvements in image acquisition and analysis procedures based on a birefringence imaging system (PolScope) that we developed for biomedical applications.[13,14] The system measures distributions of linear birefringence by use of a liquid-crystal universal compensator invented by Oldenbourg and Mei in 1994.[15] Currently, Cambridge Research and Instrumentation, Inc. manufactures several versions of the LC-PolScope system, such as SpindleView and StressView, for different application areas. The described algorithms can also be used with other birefringence imaging systems, such as those equipped with rotated wave plates or Faraday rotators that create the same polarization states.

2. Description of Polarized Light Microscope with Variable Retarders

Two configurations of the PolScope measurement system in a microscope are shown in Fig. 1. They contain in series a monochromatic light source, a variable elliptical polarizer, a condenser, a specimen, an objective lens, and a right- or left-circular analyzer and imaging detector [Fig. 1(a)] or a right- or left-circular polarizer in the illumination part and a variable elliptical analyzer in the imaging part [Fig. 1(b)]. The variable elliptical polarizer and analyzer can be made from a pair of liquid-crystal retarder cells with 45° between their principal axes and a linear polarizer.[15] Instead of the liquid crystals, a pair of variable compensators, such as Berek or Babinet–Soleil compensators, or a pair of electro-optical or piezo-optical modulators[16,17] can be used for this purpose.

The authors are with the Marine Biological Laboratory, Woods Hole, Massachusetts 02543-1015. The e-mail address for M. Shribak is mshribak@mbl.edu.

Received 1 September 2002; revised manuscript received 10 January 2003.

0003-6935/03/163009-09$15.00/0

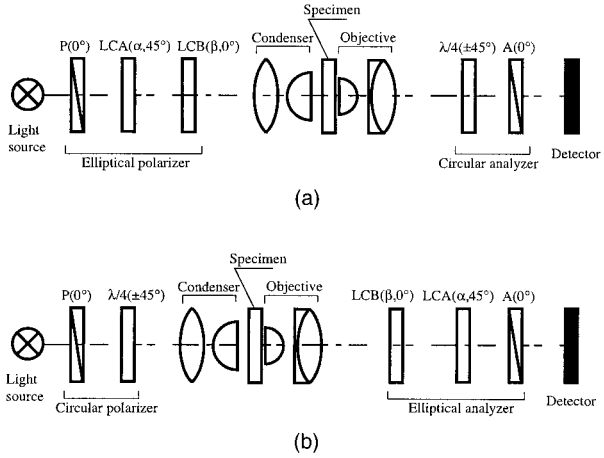

Fig. 1. Schematics of the polarized light microscope with a liquid-crystal universal compensator in the illumination path (first configuration) and in the imaging path (second configuration). α and β are the retardance of the liquid-crystal plates LCA and LCB, respectively; $\lambda/4$ is a quarter-wave plate; and P and A are the linear polarizer and analyzer.

Both configurations in Fig. 1 are described by similar equations, so we can consider one of them, for example, Fig. 1(a), with a left-circular analyzer. In the special case when the second cell LCB in Fig. 1 has quarter-wave retardance, the elliptical polarizer works as a linear polarizer with a variable azimuth. The azimuth or polarization direction equals half of the retardance, in degree, to which the first cell LCA in Fig. 1 is set. In the same way the elliptical analyzer can work as a rotated linear analyzer. A device with a rotating linear polarizer has been patented by Glazer and Cosier in 1997[18] and is described in Ref. 7.

Let us assume that the specimen has a distribution of retardance magnitudes $\Delta(x, y)$ and of slow axis directions (azimuth) $\phi(x, y)$. The retardance value Δ lies between 0° and 180°. The slow axis azimuth ranges from 0° to 180°. We use the Cartesian coordinates (x, y) to describe the magnitude and azimuth distributions in the image plane. We use the Jones calculus to simulate polarization-sensitive components in the optical train of Fig. 1. We multiply the corresponding Jones matrices for the linear polarizer, the liquid-crystal variable retarders, the specimen, the quarter-wave plate, and the linear analyzer to derive the following expression for the intensity distribution $I(\alpha, \beta, x, y)$ in the specimen image:

$$\begin{aligned} I(\alpha, \beta, x, y) = \frac{1}{2}\tau(x, y) I_{\max}(x, y)[1 \\ + \sin\alpha\cos\beta\cos\Delta(x, y) \\ - \sin\alpha\sin\beta\cos 2\phi(x, y) \\ \times \sin\Delta(x, y) \\ + \cos\alpha\sin 2\phi(x, y)\sin\Delta(x, y)] \\ + I_{\min}(x, y). \end{aligned} \tag{1}$$

Here $I_{\max}(x, y)$ is the distribution of the illumination intensity on the sample and $\tau(x, y)$ is the distribution of the isotropic specimen transparency. We also added the term $I_{\min}(x, y)$ to describe the distribution of the depolarized background illumination. All three quantities can vary over the image plane (x, y). The depolarized component represents the part of the light intensity that is unpolarized, and it therefore remains constant and contributes equally to images recorded with different settings of the variable retarders. The unpolarized light component is usually due to imperfect polarizers and optical elements that introduce polarization aberrations.[19] $I_{\min}(x, y)$ corresponds to a constant offset of the intensity signal. When images are recorded with an electronic camera, $I_{\min}(x, y)$ also includes the offset of the electronic signal that is produced in the camera by the recorded light intensity. The depolarized component is also caused by excessive scattering (multiple scattering) in turbid samples, scattering light on dust particles and scratches in an optical system, nonperfections of wave plates and liquid-crystal cells, nonzero spectral width of illumination, multiple reflections in the optical system, and nonflatness of a beam wave front while passing through optical polarization elements.

To measure the distribution of specimen magnitude $\Delta(x, y)$ and azimuth $\phi(x, y)$, we record several images at different values of retardance α and β of the variable retarders. The Jones vector of the illumination beam is determined by the following formula:

$$\mathbf{E} = \begin{bmatrix} \cos\frac{\alpha}{2}\exp\left(-i\frac{\beta}{2}\right) \\ -i\sin\frac{\alpha}{2}\exp\left(i\frac{\beta}{2}\right) \end{bmatrix}. \tag{2}$$

From here we can find the parameters of the vibration ellipse:

$$\begin{aligned} \tan 2\gamma &= \tan\alpha\sin\beta, \\ \sin 2\epsilon &= -\sin\alpha\cos\beta, \end{aligned} \tag{3}$$

where γ is the angle ($0° \le \gamma < 180°$) that the major axis makes with 0, X, and $\epsilon(-45° \le \epsilon \le 45°)$ is an auxiliary angle that specifies the shape (ellipticity) of the vibration ellipse:

$$\tan\epsilon = \frac{b}{a}. \tag{4}$$

Here a and b are the major and minor semiaxes of the ellipse, respectively.

3. Data Processing Algorithms

A. Polarization Settings of the Illumination Beam

For the measurement, a swing χ is applied to nominal retardance values of the retarders $\alpha = 90°$ and $\beta = 180°$. The following polarization settings can be used: $\Sigma_0(\alpha = 90°, \beta = 180°)$, $\Sigma_1(\alpha = 90° - \chi, \beta =$

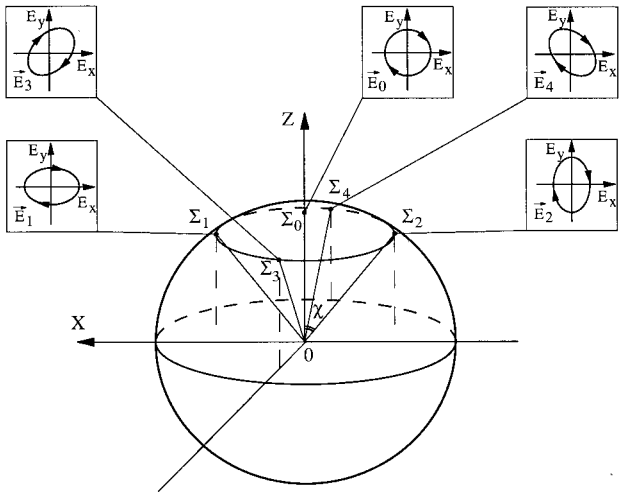

Fig. 2. Settings of the probe beam on the Poincaré sphere. Σ_0 is the setting with right-circular polarization; Σ_1, Σ_2, Σ_3, and Σ_4 are settings with elliptical polarizations. Diagrams show orientation and shape of vibration ellipsis with components E_x and E_y.

180°), $\Sigma_2(\alpha = 90° + \chi, \beta = 180°)$, $\Sigma_3(\alpha = 90°, \beta = 180° - \chi)$, $\Sigma_4(\alpha = 90°, \beta = 180° + \chi)$.

As follows from Eqs. (3) and (4), the base setting Σ_0 of the variable retarder pair creates the right-circularly polarized beam ($\epsilon = 45°$, $b/a = 1$). The four other settings make elliptically polarized beams of equal ellipticity:

$$\epsilon = 45° - \chi/2, \tag{5}$$

but with different azimuths of the major axis: $\gamma_1 = 0°$, $\gamma_2 = 90°$, $\gamma_3 = 45°$, $\gamma_4 = 135°$. A left-circular analyzer is used in this case. Thus, for the base setting, the light intensity on the imaging detector is minimal when no birefringent specimen object is present. So the setting can be called the extinction setting.

For small swing values, Eq. (4) can be approximated by

$$\frac{b}{a} = 1 - \frac{\pi}{180°}\chi, \tag{6}$$

where χ is in degrees.

The swing value that is chosen for the measurement depends on the magnitude of the prevailing specimen retardance. To measure small retardance values such as those found in living cells, χ is typically around 10°. In this case the ratio of the principal axes equals 0.82, and the ellipticity angle ϵ is 40°.

If the swing value χ is 90°, then ellipticity ϵ equals 0°. Thus the polarizations of the four illumination beam settings are linear with azimuths 0°, 45°, 90°, and 135°, respectively. Hence, our analysis can also be applied by use of a device with a rotating linear polarizer and a circular analyzer and a device with a circular polarizer and a rotating linear analyzer.

The Poincaré sphere (Fig. 2) illustrates the polarization states of the probe beam that can be used to capture the raw images. The extinction setting Σ_0 ($\alpha = 90°$, $\beta = 180°$) corresponds to the north pole of the sphere. Points that lie on a cone with axis 0, Z and the same latitude angle $90° - \chi$ describe the four other settings $\Sigma_1(\alpha = 90° - \chi, \beta = 180°)$, $\Sigma_2(\alpha = 90° + \chi, \beta = 180°)$, $\Sigma_3(\alpha = 90°, \beta = 180° - \chi)$, and $\Sigma_4(\alpha = 90°, \beta = 180° + \chi)$ with longitude angles 0°, 180°, 90°, and 270°, respectively.

In the same manner the combination of the base setting at the south pole of the Poincaré sphere with left-circular polarization of the probe beam and a right-circular analyzer can be employed. Corresponding settings of the variable retarder pair are as follows: $\Sigma_0'(\alpha = 90°, \beta = 0°)$, $\Sigma_1'(\alpha = 90° - \chi, \beta = 0°)$, $\Sigma_2'(\alpha = 90° + \chi, \beta = 0°)$, $\Sigma_3'(\alpha = 90°, \beta = -\chi)$, $\Sigma_4'(\alpha = 90°, \beta = \chi)$ or $\Sigma_0''(\alpha = 270°, \beta = 180°)$, $\Sigma_1''(\alpha = 270° - \chi, \beta = 180°)$, $\Sigma_2''(\alpha = 270° + \chi, \beta = 180°)$, $\Sigma_3''(\alpha = 270°, \beta = 180° - \chi)$, $\Sigma_4''(\alpha = 270°, \beta = 180° + \chi)$.

Intensities of the light $I(x, y, \alpha, \beta)$ on the detector for each of the polarization settings Σ_0, Σ_1, Σ_2, Σ_3, and Σ_4 with right-circular polarization of the probe beam and a left-circular analyzer can be found from Eq. (1):

$$\begin{aligned}
I_0(x, y) &= \frac{1}{2}\tau(x, y)I_{\max}[1 - \cos\Delta(x, y)] + I_{\min}(x, y),\\
I_1(x, y) &= \frac{1}{2}\tau(x, y)I_{\max}[1 - \cos\chi\cos\Delta(x, y)\\
&\quad + \sin\chi\sin 2\phi(x, y)\sin\Delta(x, y)]\\
&\quad + I_{\min}(x, y),\\
I_2(x, y) &= \frac{1}{2}\tau(x, y)I_{\max}[1 - \cos\chi\cos\Delta(x, y)\\
&\quad - \sin\chi\sin 2\phi(x, y)\sin\Delta(x, y)]\\
&\quad + I_{\min}(x, y),\\
I_3(x, y) &= \frac{1}{2}\tau(x, y)I_{\max}[1 - \cos\chi\cos\Delta(x, y)\\
&\quad - \sin\chi\cos 2\phi(x, y)\sin\Delta(x, y)]\\
&\quad + I_{\min}(x, y),\\
I_4(x, y) &= \frac{1}{2}\tau(x, y)I_{\max}[1 - \cos\chi\cos\Delta(x, y)\\
&\quad + \sin\chi\cos 2\phi(x, y)\sin\Delta(x, y)]\\
&\quad + I_{\min}(x, y).
\end{aligned} \tag{7}$$

The described formulas can also be applied for measurement systems other than those that use variable retarders because the same polarization states of the beam can be created by other polarization elements. For example, a linear polarizer followed by a quarter-wave plate with each device having an independently variable azimuth can be used to create the same polarization states.

B. Original Four-Frame Algorithm

Originally the extinction setting Σ_0 and elliptical polarization settings Σ_1, Σ_2, and Σ_3 were used in the measurement.[13] First we look for differences between image intensities I_0, I_1, I_2, and I_3:

$$\begin{aligned} I_1 - I_2 &= \tau I_{\max} \sin\chi \sin 2\phi \sin\Delta, \\ I_1 + I_2 - 2I_3 &= \tau I_{\max} \sin\chi \cos 2\phi \sin\Delta, \\ I_1 + I_2 - 2I_0 &= \tau I_{\max}(1 - \cos\chi)\cos\Delta. \end{aligned} \tag{8}$$

As stated above, the values of Δ and ϕ lie between 0° and 180°. That means that $\sin\Delta \geq 0$ and

$$\begin{aligned} 0° \leq \Delta \leq 90° \qquad & \text{when } I_1 + I_2 - 2I_0 \geq 0, \\ 90° < \Delta < 180° \qquad & \text{when } I_1 + I_2 - 2I_0 < 0, \\ 0° \leq \phi \leq 90° \qquad & \text{when } I_1 - I_2 \geq 0, \\ 90° < \phi < 180° \qquad & \text{when } I_1 - I_2 < 0. \end{aligned} \tag{9}$$

Then the following two terms are calculated:

$$\begin{aligned} A &\equiv \frac{I_1 - I_2}{I_1 + I_2 - 2I_0} \tan\frac{\chi}{2} = \sin 2\phi \tan\Delta, \\ B &\equiv \frac{I_1 + I_2 - 2I_3}{I_1 + I_2 - 2I_0} \tan\frac{\chi}{2} = \cos 2\phi \tan\Delta. \end{aligned} \tag{10}$$

From here we find expressions for the retardance Δ and azimuth ϕ:

$$\begin{aligned} &\Delta = \arctan[(A^2 + B^2)^{1/2}] \qquad \text{when } I_1 + I_2 - 2I_0 \geq 0, \\ &\Delta = 180° - \arctan[(A^2 + B^2)^{1/2}] \\ &\qquad\qquad \text{when } I_1 + I_2 - 2I_0 < 0, \\ &\phi = \frac{1}{2}\arctan\left(\frac{A}{B}\right). \end{aligned} \tag{11}$$

The above formulas for the magnitude and slow axis direction of specimen retardance apply to transparent specimens that possess linear birefringence.

C. Correction of Background Retardance

When measuring small specimen retardances, it is important to consider the spurious differential transmission and phase shift contributed by optical components such as lenses and optical flats that are located between the polarizer and the analyzer of the measurement system. Despite careful selection of optical components with minimal strain, there typically remains some polarization distortions that are due to, for example, high numerical aperture lens surfaces (for techniques to rectify polarization distortions, see Ref. 19). In an imaging system, the polarization distortions contributed by instrument components lead to a variation in the differential phase shift across the imaged field. The spatially varying differential phase shift, or background retardance, leads to systematic errors in the measurement of specimen retardances. The systematic errors are especially intruding if object retardances are of the same magnitude or smaller than the background retardance.

We developed a correction procedure to minimize errors that are due to background retardance. The procedure is based on specimen images that are recorded with no birefringent object in the optical path. Typically, to record the background set of images, the object is moved out of the field of view of the camera by use of the x–y translator on the specimen stage of the microscope. Except for this lateral displacement to view an empty region of the specimen preparation, all other settings, including focus, are kept the same as those used for recording the object images. In particular, background images are captured with the same compensator settings as for the object itself. We call the background set of images I_{bg0}, I_{bg1}, I_{bg2}, I_{bg3}, and I_{bg4}.

The background images are used to remove the contribution of the background retardance from object images. This works particularly well when retardance magnitude values of the background and the object are small. For a mathematical treatment of the background retardance that superimposes on the object retardance, we assume that both anisotropies are placed in series and we form the matrix product of their respective Jones matrices $\mathbf{M}_o$ (object) and $\mathbf{M}_b$ (background):

$$\mathbf{M}_o \cdot \mathbf{M}_b, \qquad \text{or } \mathbf{M}_b \cdot \mathbf{M}_o, \tag{12}$$

where

$$\mathbf{M}_o = \begin{bmatrix} \cos\frac{\Delta_o}{2} + i\sin\frac{\Delta_o}{2}\cos 2\phi_o & i\sin\frac{\Delta_o}{2}\sin 2\phi_o \\ i\sin\frac{\Delta_o}{2}\sin 2\phi_o & \cos\frac{\Delta_o}{2} - i\sin\frac{\Delta_o}{2}\cos 2\phi_o \end{bmatrix} \approx \begin{bmatrix} 1 + \frac{i}{2}\Delta_o\cos 2\phi_o & \frac{i}{2}\Delta_o\sin 2\phi_o \\ \frac{i}{2}\Delta_o\sin 2\phi_o & 1 - \frac{i}{2}\Delta_o\cos 2\phi_o \end{bmatrix},$$

$$\mathbf{M}_b = \begin{bmatrix} \cos\frac{\Delta_b}{2} + i\sin\frac{\Delta_b}{2}\cos 2\phi_b & i\sin\frac{\Delta_b}{2}\sin 2\phi_b \\ i\sin\frac{\Delta_b}{2}\sin 2\phi_b & \cos\frac{\Delta_b}{2} - i\sin\frac{\Delta_b}{2}\cos 2\phi_b \end{bmatrix} \approx \begin{bmatrix} 1 + \frac{i}{2}\Delta_b\cos 2\phi_b & \frac{i}{2}\Delta_b\sin 2\phi_b \\ \frac{i}{2}\Delta_b\sin 2\phi_b & 1 - \frac{i}{2}\Delta_b\cos 2\phi_b \end{bmatrix}.$$

For both of the Jones matrices we assumed that the magnitude of the specimen retardance Δ_o and of the

background retardance Δ_b are small. Therefore we expanded their sine and cosine functions and kept only the linear terms, as shown on the right side of the equations. After forming the matrix product, we again retain only the linear terms and obtain

$$\mathbf{M}_o \cdot \mathbf{M}_b = \mathbf{M}_b \cdot \mathbf{M}_o = \begin{bmatrix} 1 + \frac{i}{2}(\Delta_o \cos 2\phi_o + \Delta_b \cos 2\phi_b) & \frac{i}{2}(\Delta_o \sin 2\phi_o + \Delta_b \sin 2\phi_b) \\ \frac{i}{2}(\Delta_o \sin 2\phi_o + \Delta_b \sin 2\phi_b) & 1 - \frac{i}{2}(\Delta_o \cos 2\phi_o + \Delta_b \cos 2\phi_b) \end{bmatrix}. \quad (13)$$

This result indicates that the terms $\Delta_{o,b} \sin 2\phi$ and $\Delta_{o,b} \cos 2\phi$ are additive when both retardances are placed in series.

In an experiment, we observe an object superimposed on the background retardance that together are expressed by the experimental matrix $\mathbf{M}_e$:

$$\mathbf{M}_e = \begin{bmatrix} 1 + \frac{i}{2}\Delta_e \cos 2\phi_e & \frac{i}{2}\Delta_e \sin 2\phi_e \\ \frac{i}{2}\Delta_e \sin 2\phi_e & 1 - \frac{i}{2}\Delta_e \cos 2\phi_e \end{bmatrix}. \quad (14)$$

Comparing the matrix $\mathbf{M}_e$ and the matrix product $\mathbf{M}_o \cdot \mathbf{M}_b$, we can write

$$\begin{aligned} \Delta_e \sin 2\phi_e &= \Delta_o \sin 2\phi_o + \Delta_b \sin 2\phi_b, \\ \Delta_e \cos 2\phi_e &= \Delta_o \cos 2\phi_o + \Delta_b \cos 2\phi_b. \end{aligned} \quad (15)$$

Hence we can find the object parameters by subtracting the measured background parameters from the experimental data:

$$\begin{aligned} \Delta_o \sin 2\phi_o &= \Delta_e \sin 2\phi_e - \Delta_b \sin 2\phi_b, \\ \Delta_o \cos 2\phi_o &= \Delta_e \cos 2\phi_e - \Delta_b \cos 2\phi_b. \end{aligned} \quad (16)$$

Let us then turn to Eqs. (10) and recognize that the terms $\Delta \sin 2\phi$ and $\Delta \cos 2\phi$ correspond to the expressions for A and B, respectively, noting that $\tan \Delta \approx \Delta$, if Δ is small. Hence, if A and B designate the values measured with the object in place and A_{bg} and B_{bg} are the values without an object (i.e., background), then $A - A_{\mathrm{bg}}$ and $B - B_{\mathrm{bg}}$ represent the values of the object alone, as if it were measured without background retardance.

On the basis of these insights, we devised the following background correction procedure when imaging objects with low-retardance magnitude:

1. Record the image set with the birefringent object in the viewing area.
2. Translate the specimen to the side to view the clear specimen area.
3. Record the image set of the clear area to document background retardance.
4. Calculate and store intermediate results A_{bg} and B_{bg}.
5. When calculating object retardances, subtract A_{bg} and B_{bg} from intermediate results A and B and use background-corrected values to calculate the object retardance magnitude and azimuth.

In addition to correcting for spurious differential absorption and phase shift, this procedure also accounts for small differences in the individual swing values χ used for each of the settings $\Sigma_1(\alpha = 90° - \chi, \beta = 180°)$, $\Sigma_2(\alpha = 90° + \chi, \beta = 180°)$, $\Sigma_3(\alpha = 90°, \beta = 180° - \chi)$, and $\Sigma_4(\alpha = 90°, \beta = 180° + \chi)$. Slight drifts in the calibration of the liquid crystals due to temperature changes, for example, might cause small differentials in the effective swing values for Σ_1, Σ_2, Σ_3, and Σ_4. Those small differentials can be mathematically treated as a small and uniform background retardance. As a result, the above background correction procedure will also remove errors in the measured object retardance caused by a slight miscalibration of settings Σ_1, Σ_2, Σ_3, and Σ_4.

Typically, the background retardance does not change appreciably over a time period of many minutes or even hours. Therefore the intermediate results A_{bg} and B_{bg} can be used repeatedly to correct, e.g., a time series of sample images measuring the subtle changes in birefringence in a living cell.

D. Three-Frame Algorithm without Extinction Setting

It is possible to use three elliptically polarized settings Σ_1, Σ_2, and Σ_3 in case of moderate extinction ratio ($I_{\max}/I_{\min} > 200$) of the microscope. We can neglect $I_{\min}$ and use the following formulas for data processing:

$$\begin{aligned} A &\equiv \frac{I_1 - I_3}{I_1 + I_2} = \frac{1}{\sqrt{2}} \frac{\sin \chi}{1 - \cos \chi \cos \Delta} \sin(2\phi + 45°) \sin \Delta, \\ B &\equiv \frac{I_2 - I_3}{I_1 + I_2} = \frac{1}{\sqrt{2}} \frac{\sin \chi}{1 - \cos \chi \cos \Delta} \cos(2\phi + 45°) \sin \Delta. \end{aligned} \quad (17)$$

Retardance and azimuth distributions can be calculated in the following way:

$$\begin{aligned} \Delta &= 2 \arctan\left\{ \frac{[2(A^2 + B^2)]^{1/2}}{1 + [1 - 2(A^2 + B^2)]^{1/2}} \tan \frac{\chi}{2} \right\}, \\ \phi &= \frac{1}{2} \arctan\left(\frac{A}{B}\right) - 22.5°. \end{aligned} \quad (18)$$

This technique has approximately the same sensitivity as the previous technique; and because of the reduced number of frames, it permits an increase in

the speed of measurement. Moreover, a correction of the background retardance that is similar to the one described in Subsection 3.C can be used here.

E. Five-Frame Algorithm

Use of the additional elliptically polarized setting Σ_4 that is complimentary to the third elliptical setting Σ_3 allows us to increase the sensitivity and make it equal for all azimuth values of the specimen. In this case the following formulas for terms A and B are used:

$$A \equiv \frac{I_1 - I_2}{I_1 + I_2 - 2I_0} \tan\frac{\chi}{2} = \sin 2\phi \tan\Delta,$$
$$B \equiv \frac{I_4 - I_3}{I_4 + I_3 - 2I_0} \tan\frac{\chi}{2} = \cos 2\phi \tan\Delta. \quad (19)$$

Then the retardance and azimuth can be found as

$$\Delta = \arctan[(A^2 + B^2)^{1/2}] \quad \text{when } I_1 + I_2 - 2I_0 \geq 0,$$
$$\Delta = 180^\circ - \arctan[(A^2 + B^2)^{1/2}] \quad \text{when } I_1 + I_2 - 2I_0 < 0,$$
$$\phi = \frac{1}{2}\arctan\left(\frac{A}{B}\right). \quad (20)$$

The background correction procedure described in Subsection 3.C can be applied here as well.

F. Four-Frame Algorithm without Extinction Setting

When using a microscope with moderate extinction ratio ($I_{max}/I_{min} > 200$), we can eliminate the circularly polarized setting Σ_0 and use the four elliptical settings only. The processing formulas become more complicated:

$$A \equiv \frac{I_1 - I_2}{I_1 + I_2} = \frac{\sin\chi}{1 - \cos\chi\cos\Delta} \sin 2\phi \sin\Delta,$$
$$B \equiv \frac{I_4 - I_3}{I_4 + I_3} = \frac{\sin\chi}{1 - \cos\chi\cos\Delta} \cos 2\phi \sin\Delta. \quad (21)$$

From here we calculate the following retardance and azimuth distributions:

$$\Delta = 2\arctan\left\{\frac{(A^2 + B^2)^{1/2}}{1 + [1 - (A^2 + B^2)]^{1/2}} \tan\frac{\chi}{2}\right\},$$
$$\phi = \frac{1}{2}\arctan\left(\frac{A}{B}\right). \quad (22)$$

This technique has the same advantages as the five-frame method. Also, both techniques are less sensitive to system imperfections, and a correction of the background retardance similar to the one described in Subsection 3.C can be used here as well.

G. Two-Frame Algorithm

For fast measurements of low-retardance specimens, we propose the following algorithm. Images are captured with two elliptical settings Σ_1 and Σ_3 with azimuths of 0° and 45°. For the calculation we need two images I_1 and I_3 [see Eqs. (7)] with the specimen in the microscope field and at least one background image, for example, with the first elliptical setting I_{bg1}, without the specimen in the field:

$$I_1(x, y) = \frac{1}{2} I_{max}[1 - \cos\chi\cos\Delta(x, y) + \sin\chi\sin 2\phi(x, y)\sin\Delta(x, y)] + I_{min}(x, y),$$
$$I_3(x, y) = \frac{1}{2} I_{max}[1 - \cos\chi\cos\Delta(x, y) - \sin\chi\cos 2\phi(x, y)\sin\Delta(x, y)] + I_{min}(x, y),$$
$$I_{bg1}(x, y) = I_{max}\sin^2\frac{\chi}{2} + I_{min}(x, y). \quad (23)$$

Here we assume $\tau(x, y) = 1$. In case of small retardance we can use the following expressions:

$$A \equiv \frac{I_1 - I_{bg1}}{I_{bg1}} \tan\frac{\chi}{2} \approx \sin 2\phi \sin\Delta,$$
$$B \equiv \frac{I_3 - I_{bg1}}{I_{bg1}} \tan\frac{\chi}{2} \approx \cos 2\phi \sin\Delta. \quad (24)$$

However, in practical cases background pictures at different elliptical settings are not exactly the same, for reasons explained in Subsection 3.C. Therefore, instead of I_{bg1} in the term B, it is better to use the correspondent background image I_{bg3}. To take into account depolarized illumination and the constant component in the signals, we can use the background picture at the extinction setting I_{bg0}. So in practice it is better to use the three background images I_{bg0}, I_{bg1}, and I_{bg3}:

$$A \equiv \frac{I_1 - I_{bg1}}{I_{bg1} - I_{bg0}} \tan\frac{\chi}{2} \approx \sin 2\phi \sin\Delta,$$
$$B \equiv \frac{I_3 - I_{bg3}}{I_{bg3} - I_{bg0}} \tan\frac{\chi}{2} \approx \cos 2\phi \sin\Delta. \quad (25)$$

Then the retardance and azimuth can be found as

$$\Delta = \arcsin[(A^2 + B^2)^{1/2}] \approx \frac{\lambda}{2\pi}(A^2 + B^2)^{1/2},$$
$$\phi = \frac{1}{2}\arctan\left(\frac{A}{B}\right). \quad (26)$$

Here λ is the wavelength of the illuminating light.

As mentioned above, we derived the formulas using linear approximations for trigonometric functions. They give wholly satisfactory results for specimens with small retardance. The main advantage of the technique lies in the fact that only two images of a

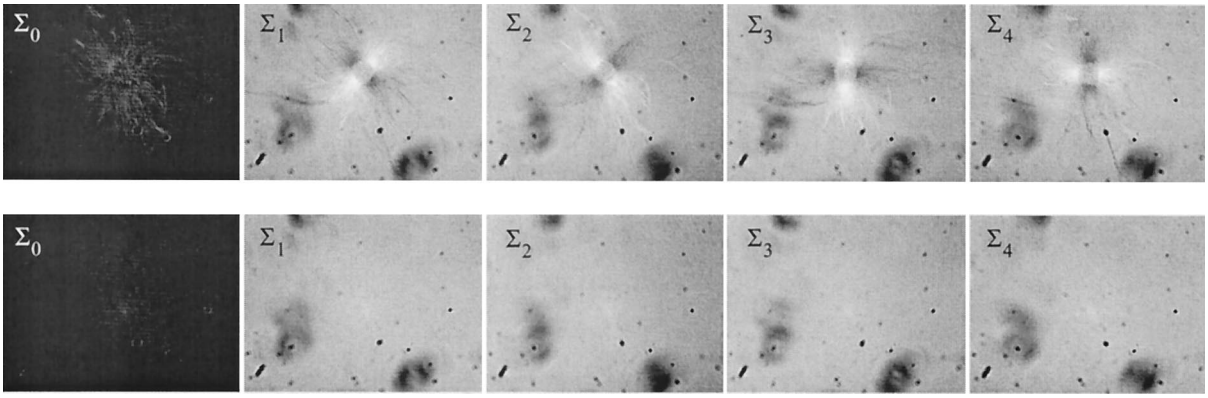

Fig. 3. Five intensity images of aster (top) and background (bottom) at polarization settings Σ_0, Σ_1, Σ_2, Σ_3, and Σ_4 of the universal compensator. The images were contrast enhanced for better visibility.

birefringent object are needed to receive a map of retardance and azimuth distributions.

If the illumination beam is linearly polarized with azimuths of 0° and 45° (swing χ equals 90°), we can obtain an exact retardance value:

$$\Delta = \arcsin[(A^2 + B^2)^{1/2}]. \tag{27}$$

The sensitivity of this technique, however, is less then the four-frame and five-frame measurements.

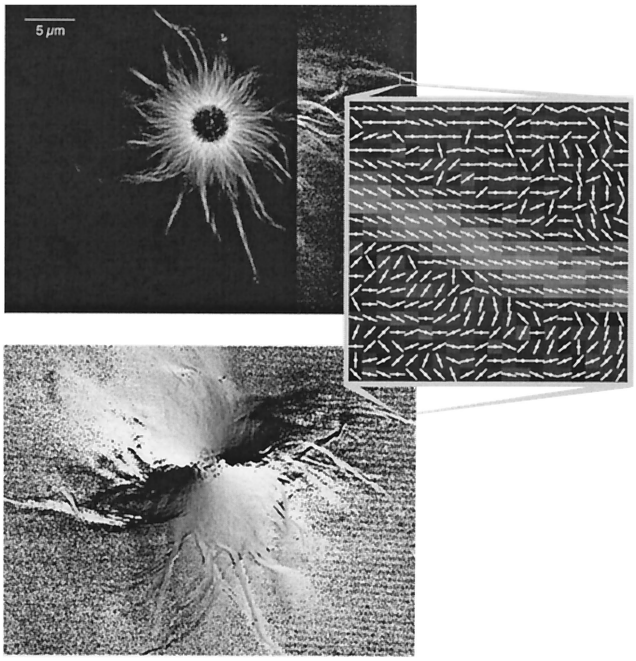

Fig. 4. Reconstituted aster consisting of microtubules that were polymerized off a spherical organizing center called centrosome. Top left image: retardance magnitude image calculated with the five-frame algorithm with background correction. Bright microtubule arrays and bundles radiate from the dark centrosome. White corresponds to 1.2-nm birefringence retardation; black corresponds to zero birefringence. The right portion of the image is contrast enhanced to improve the visibility of fine fibers and the background noise. Bottom left image: orientation of the birefringence axis recorded with the PolScope. Black corresponds to horizontal orientation; increasing brightness corresponds to increasing orientation angles measured from the horizontal direction. Inset: enlarged region showing a microtubule bundle. The magnitude image is overlaid by lines indicating the orientation of the measured birefringence axis in each pixel. In pixels representing the microtubule bundle, the birefringence axis (high-refractive-index axis) is parallel to the bundle.

4. Experimental Verification

To experimentally analyze the data processing algorithms, we used a polarized light microscope with a liquid-crystal universal compensator described in more detail in Ref. 20. Briefly, a microscope stand (Microphot SA from Nikon, Melville, New York) was equipped with polarization components according to the scheme shown in Fig. 1(a). Two liquid-crystal variable retarders LCA and LCB (Fig. 1) (Cambridge Research and Instrumentation, Inc.) were placed in the illumination path following the linear polarizer. The analyzer for circularly polarized light was placed in the illumination path after the objective lens. We used a 60×/1.4 numerical aperture Plan-Apochromat objective lens and an apochromat oil immersion condenser lens, both selected for low-polarization aberrations (Nikon); a high-pressure mercury arc lamp followed by an Ellis light scrambler (Technical Video, Woods Hole, Massachusetts) as the light source; and a narrow-bandpass interference filter (546 nm, 12-nm FWHM; Omega, Brattleboro, Vermont) to select the green mercury line for intense monochromatic illumination. We captured the images with a scientific-grade video CCD camera (C300 from Dage, Michigan City, Indiana) and digitized at 8 bits/pixel using a frame grabber board (AG-5; Scion Corp., Frederick, Maryland). We accomplished image acquisition and initial analysis using public domain image processing software (NIH Image, developed at the National Institutes of Health),[21] which was enhanced by custom-written software functions. For further image analysis, raw images were transferred to a software package developed with MATHEMATICA (Wolfram Research, Champaign,

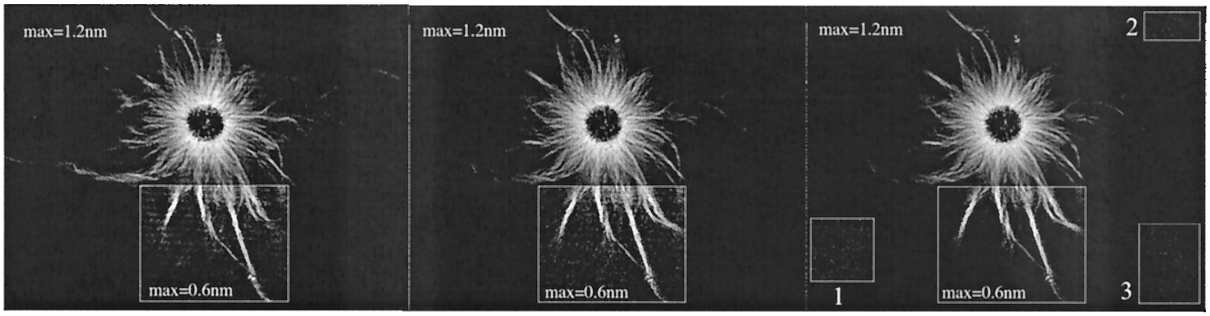

Fig. 5. Magnitude images of the aster that were calculated with (a) the two-frame, (b) the original four-frame, (c) the five-frame algorithms. In all cases a background correction was applied. White corresponds to 1.2- or 0.6-nm birefringence retardation, as shown in the areas, and black corresponds to zero birefringence. Areas 1, 2, and 3 in (c) were used for measuring the noise level. Here white corresponds to 0.3-nm retardance.

Illinois), which we used to implement the data processing algorithms described in Section 3.

For the test objects, we imaged parallel arrays of stiff biopolymers that radiate from a common organizing center. The objects are called asters and consist of microtubule arrays that polymerize off centrosomes, which are microtubule organizing centers found in almost all animal cells. Purified components to reconstitute asters *in vitro* were kindly provided by Robert E. Palazzo of the University of Kansas and the Marine Biological Laboratory. The preparation and purification procedures are described in Ref. 22. For this study, asters were fixed in a phosphate-buffered saline solution containing 50% glycerol and 2% glutaraldehyde. An approximate 10-μl solution containing asters was sandwiched between a microscope slide and coverslip [Nr. (standard thickness) 1 ½]. The slide–coverslip assembly that included a 25-μm-thick Mylar spacer was sealed with nail polish.

Initially we recorded five images of the specimen at polarization settings Σ_0, Σ_1, Σ_2, Σ_3, and Σ_4 of the universal compensator as described in Subsection 3.A. The recorded raw images are shown in Fig. 3. As can be seen in the top row of aster images, the raw images have poor contrast and spurious background features. The background features are also visible in the bottom row of images shown in Fig. 3.

Subsequently, we processed the raw images using the algorithms described in Section 3. We obtained the best results using the five-frame and four-frame algorithms without extinction setting. An example of the magnitude and azimuth distributions calculated with the five-frame algorithm is shown in Fig. 4.

Figure 5 shows a comparison of magnitude images calculated by use of the two-frame, original four-frame, and five frame algorithms. The five-frame picture has the least noise and spurious artifacts when compared with the original four-frame and two-frame algorithms. The two-frame picture is most noisy but can still be used for observation of the structure. The three-frame algorithm without extinction setting yields the same result as the original four-frame technique, whereas the four-frame algorithm without extinction setting yields the same result as the five-frame procedure.

We also analyzed the noise in image areas where a birefringence object was absent. The noise is due to uncertainties in the measured pixel values of the raw intensity images. The uncertainties are mainly due to the read noise of the video-rate CCD camera and the shot noise of recorded image intensities. The examined image areas are shown in Fig. 5(c). The azimuth distributions in the considered areas are random with a mean value equal to 90°. The results of the magnitude measurements are given in Table 1. The five-frame and four-frame techniques have a noise floor of 0.036-nm retardance. Noise levels of the original four-frame and three-frame algorithms without extinction setting are 0.049 nm, which is 36% higher than the previous results. The two-frame procedure yielded a noise floor of 0.053 nm.

Table 1. Retardance Noise Levels Generated by the Different Algorithms

Number of Frames Used in Algorithm	Noise Level (nm)			
	Area 1	Area 2	Area 3	Average
Two	0.051	0.051	0.057	0.053
Three	0.047	0.047	0.052	0.049
Four (original)	0.048	0.048	0.052	0.049
Four (without extinction)	0.035	0.035	0.038	0.036
Five	0.035	0.035	0.038	0.036

5. Conclusion

Various configurations of the polarized light microscope with a universal compensator are used for biomedical and other applications. Here we are proposing different image acquisition and processing algorithms to address different requirements for speed and accuracy for the measurement of two-dimensional distributions of linear birefringence. The highest accuracy can be achieved with the five-frame technique and the four-frame algorithm with-

out extinction setting. To observe specimens with fast-moving objects, the two-frame algorithm can be useful. The algorithms can be employed for polarization imaging systems by use of different optical configurations including variable retarders such as liquid-crystal and electro-optical plates, fixed retarders with variable azimuth, and Faraday rotators.

The authors thank S. Inoué of the Marine Biological Laboratory for helpful discussions and comments on this research. We also thank Robert E. Pallazzo and Craig Steeds of the University of Kansas for help in specimen preparation. This research was funded by the National Institutes of Health grant GM49210.

References

1. S. Inoué, *Video Microscopy* (Plenum, New York, 1986).
2. S. Inoué and R. Oldenbourg, "Microscopes," in *Handbook of Optics*, 2nd ed., M. Bass, ed. (McGraw-Hill, New York, 1995), Vol. 2, pp. 17.1–17.52.
3. M. Noguchi, T. Ishikawa, M. Ohno, and S. Tachihara, "Measurement of 2D birefringence distribution," in *International Symposium on Optical Fabrication, Testing, and Surface Evaluation*, J. Tsujiuchi, ed., Proc. SPIE **1720,** 367–378 (1992).
4. Y. Otani, T. Shimada, T. Yoshizawa, and N. Umeda, "Two-dimensional birefringence measurement using the phase shifting technique," Opt. Eng. **33,** 1604–1609 (1994).
5. J. L. Pezzanitti and R. A. Chipman, "Mueller matrix imaging polarimetry," Opt. Eng. **34,** 1558–1568 (1995).
6. A. L. Bajor, "Automated polarimeter-macroscope for optical mapping of birefringence, azimuths, and transmission in large area wafer. Part I. Theory of the measurement," Rev. Sci. Instrum. **66,** 2977–2990 (1995).
7. A. M. Glazer, J. G. Lewis, and W. Kaminsky, "An automatical optical imaging system for birefringent media," Proc. R. Soc. London Ser. A **452,** 2751–2765 (1996).
8. Y. Zhu, T. Koyama, T. Takada, and Y. Murooka, "Two-dimensional measurement technique for birefringence vector distributions: measurement principle," Appl. Opt. **38,** 2225–2231 (1999).
9. Y. Zhu, T. Takada, and Y. Murooka, "Two-dimensional optical measurement techniques based on optical birefringence effects," Opt. Eng. **41,** 3183–3192 (2002).
10. M. I. Shribak, "Autocollimating detectors of birefringence," in *International Conference on Optical Inspection and Micromeasurements*, C. Gorecki, ed., Proc. SPIE **2782,** 805–813 (1996).
11. M. I. Shribak, Y. Otani, and T. Yoshizawa, "Return-path polarimeter for two-dimensional birefringence distribution measurement," in *Polarization: Measurement, Analysis, and Remote Sensing II*, D. H. Goldstein and D. B. Chenault, eds., Proc. SPIE **3754,** 144–149 (1999).
12. W. H. Yeh, J. Carrier, and M. Mansuripur, "Polarization microscopy of magnetic domains for magneto-optical disks," Appl. Opt. **38,** 3749–3758 (1999).
13. G. Mei and R. Oldenbourg, "Fast imaging polarimetry with precision universal compensator," in *Polarization Analysis and Measurement II*, D. H. Goldstein and D. B. Chenault, eds., Proc. SPIE **2265,** 29–39 (1994).
14. R. Oldenbourg and G. Mei, "New polarized light microscope with precision universal compensator," J. Microsc. (Oxford) **180,** 140–147 (1995).
15. R. Oldenbourg and G. Mei, "Polarized light microscopy," U.S. patent 5,521,705 (12 May 1994). Patent is licensed to Cambridge Research and Instrumentation, Inc., Woburn, Mass.; http://www.cri-inc.com.
16. T. Yamaguchi, S. Yoshida, and A. Kinbara, "Continuous ellipsometric determination of the optical constants and thickness of a silver film during deposition," Jpn. J. Appl. Phys. **8,** 559–567 (1969).
17. P. S. Hauge, "Recent developments in instrumentation in ellipsometry," Surf. Sci. **96,** 108–140 (1980).
18. A. M. Glazer and J. Cosier, "Method and apparatus for indicating optical anisotropy," UK patent application 2,310,925 (7 February 1997).
19. M. Shribak, S. Inoué, and R. Oldenbourg, "Polarization aberrations caused by differential transmission and phase shift in high NA lenses: theory, measurement and rectification," Opt. Eng. **41,** 943–954 (2002).
20. R. Oldenbourg, E. D. Salmon, and P. T. Tran, "Birefringence of single and bundled microtubules," Biophys. J. **74,** 645–654 (1998).
21. The NIH Image software is available at http://rsb.info.nih.gov/NIH-image.
22. B. J. Schnackenberg and R. E. Palazzo, "Reconstitution of centrosome microtubule nucleation in Spisula," Methods Cell Biol. **67,** 149–165 (2001).